The Astrophysical Journal, 967:22 (18pp), 2024 May 20 https://doi.org/10.3847/1538-4357/ad32c7

Resolved Near-infrared Stellar Photometry from the Magellan Telescope for 13 Nearby Galaxies: J-region Asymptotic Giant Branch Method Distances

Abigail J. Lee[1,2], Andrew J. Monson[3], Wendy L. Freedman[1,2], Barry F. Madore[1,4], Kayla A. Owens[1,2], Rachael L. Beaton[5,6], Coral Espinoza[1,7], Tongtian Ren[8], and Yi Ren[9]
[1] Department of Astronomy & Astrophysics, University of Chicago, 5640 South Ellis Avenue, Chicago, IL 60637, USA; abbyl@uchicago.edu
[2] Kavli Institute for Cosmological Physics, University of Chicago, 5640 South Ellis Avenue, Chicago, IL 60637, USA
[3] Steward Observatory, The University of Arizona, 933 North Cherry Avenue, Tucson, AZ 85721, USA
[4] Observatories of the Carnegie Institution for Science, 813 Santa Barbara Street, Pasadena, CA 91101, USA
[5] Space Telescope Science Institute, Baltimore, MD 21218, USA
[6] Department of Physics and Astronomy, Johns Hopkins University, Baltimore, MD 21218, USA
[7] Lake Forest College Physics Department, Lake Forest, IL 60045, USA
[8] Jodrell Bank Centre for Astrophysics, University of Manchester, Oxford Road, Manchester, M13 9PL, UK
[9] College of Physics and Electronic Engineering, Qilu Normal University, Jinan 250200, People's Republic of China
Received 2023 November 30; revised 2024 February 19; accepted 2024 February 28; published 2024 May 14

Abstract

We present near-infrared *JHK* photometry for the resolved stellar populations in 13 nearby galaxies: NGC 6822, IC 1613, NGC 3109, Sextans B, Sextans A, NGC 300, NGC 55, NGC 7793, NGC 247, NGC 5253, Cen A, NGC 1313, and M83, acquired from the 6.5 m Baade–Magellan telescope. We measure distances to each galaxy using the J-region asymptotic giant branch (JAGB) method, a new standard candle that leverages the constant luminosities of color-selected, carbon-rich AGB stars. While only single-epoch, random-phase photometry is necessary to derive JAGB distances, our photometry is time-averaged over multiple epochs, thereby decreasing the contribution of the JAGB stars' intrinsic variability to the measured dispersions in their observed luminosity functions. To cross-validate these distances, we also measure near-infrared tip of the red giant branch (TRGB) distances to these galaxies. The residuals obtained from subtracting the distance moduli from the two methods yield an rms scatter of $\sigma_{\mathrm{JAGB-TRGB}} = \pm 0.07$ mag. Therefore, all systematics in the JAGB method and TRGB method (e.g., crowding, differential reddening, star formation histories) must be contained within these ± 0.07 mag bounds for this sample of galaxies because the JAGB and TRGB distance indicators are drawn from entirely distinct stellar populations and are thus affected by these systematics independently. Finally, the composite JAGB star luminosity function formed from this diverse sample of galaxies is well described by a Gaussian function with a modal value of $M_J = -6.20 \pm 0.003$ mag (stat), indicating that the underlying JAGB star luminosity function of a well-sampled full star formation history is highly symmetric and Gaussian based on over 6700 JAGB stars in the composite sample.

Unified Astronomy Thesaurus concepts: Observational astronomy (1145); Near infrared astronomy (1093); Distance indicators (394); Asymptotic giant branch stars (2100); Carbon stars (199); Galaxy distances (590); Red giant branch (1368)

Supporting material: figure sets, machine-readable table

1. Introduction

Carbon stars were first serendipitously discovered more than 150 years ago by Father Secchi at the Vatican Observatory when he noticed the similarity in the spectra between a small group of peculiarly red stars and the light in carbon arc lights[10] (Secchi 1868). More than 100 years later, Richer (1981) laid the path for carbon stars as standard candles when he realized that the carbon star bolometric luminosity function (LF) was bright and fairly symmetric. Soon after, Cook et al. (1986) speculated that the carbon star LF could be used as a distance indicator after observing the similarities in the *I*-band LF of carbon stars in M31, M33, NGC 6822, and IC 1613. Fifteen years later, Nikolaev & Weinberg (2000) and Weinberg & Nikolaev (2001) identified a region of the near-infrared (NIR) color–magnitude diagram (CMD) populated nearly exclusively by carbon-rich asymptotic giant branch (AGB) stars (identified photometrically) and successfully used them as standard candles to probe the 3D structure of the LMC. Twenty years later, Madore & Freedman (2020a), Freedman & Madore (2020, FM20), and Ripoche et al. (2020) showed for the first time the promise of carbon stars in the *J* band for measuring extragalactic distances, where they have a constant average magnitude.

Carbon stars are theoretically predicted to be robust standard candles. Intermediate-age and intermediate-mass stars inevitably evolve onto the thermally pulsating AGB (TP-AGB), a short final phase of a star's life that lasts only $\sim 10^6$ yr (Habing & Olofsson 2003). During this phase, the star alternates between burning helium and hydrogen in shells around a degenerate carbon–oxygen core. For most (~90%) of the TP-AGB stage, the helium-burning shell is essentially dormant, while the hydrogen shell burns and rains helium ash onto the helium shell, increasing its pressure and temperature until helium fusion is eventually triggered. The helium-shell-burning phase is called a "thermal pulse" and lasts a few hundred years. As the helium shell fuses helium into carbon (via the triple-α

[10] The first practical electrical lights.

reaction), it expands, forcing the hydrogen shell layer above it to expand as well, lowering its temperature and density and thereby terminating the hydrogen shell fusion. Furthermore, the energy from the helium shell burning is now too great to be transported through the star by radiation alone, so a convective shell develops above the helium-burning region. These convective cells may also transport carbon from the inner layers of the star up to the stellar surface and enrich it. This is called the "third dredge-up event." The thermal pulse phase ends when the helium shell depletes its fuel and then contracts, which in turn increases the pressure and temperature in the hydrogen shell zone above it, retriggering hydrogen fusion. Between the thermal pulses, the star burns solely via the hydrogen shell for 10,000–100,000 yr (Habing & Olofsson 2003). The TP-AGB phase continues until the convective envelope dissipates via mass loss and the star becomes a planetary nebula and then eventually a white dwarf.

In some stars, a sufficient number of dredge-up events occur for the abundance of carbon to exceed that of oxygen on the stellar surface ($C/O > 1$),[11] and the star becomes known as "carbon-rich." Conversely, the "oxygen-rich," or M-type AGB star predecessors to C-rich AGB stars, have ratios of $C/O < 1$ in their atmospheres. C stars' spectra are dominated by bands of the C_2 and CN molecules, which increase the opacity of the AGB star's stellar atmosphere in typical photometric bandpasses and are therefore responsible for the observed cooling of the star's effective temperature and carbon stars' distinctive red color (Marigo et al. 2003). A notable dichotomy exists in the effective temperatures and NIR colors between oxygen-rich and carbon-rich AGB stars, where carbon stars are distinctively cooler and redder.

Carbon stars are also well constrained in luminosity because of the small range of masses for which the third dredge-up event is effective at forming carbon stars (≈2–4.5 $M_\odot$).[12] Hot-bottom burning occurs in stars with initial masses of $M > 4.5\ M_\odot$, where the carbon is burned into nitrogen before it can reach the stellar surface, because the star's interior is so massive and therefore too hot. Stars with initial masses of $M < 2\ M_\odot$ eject all the matter between the core and stellar surface after a few thermal pulses because the mass of the envelope was so small to begin with, and all evolution is terminated before the conversion to a carbon star can take place (Marigo et al. 2003; Kamath et al. 2023).

These theoretical predictions are reflected observationally in the low dispersion of carbon star luminosities, particularly in the NIR (0.3 mag; Weinberg & Nikolaev 2001), making these stars excellent candidates for standard candles. Aptly, carbon stars with colors of 1.5 mag $< (J - K) <$ 2.0 mag, denominated J-region AGB (JAGB) stars by Madore & Freedman (2020a), have been found to to be precise and accurate standard candles in the NIR by several different groups and papers (Weinberg & Nikolaev 2001; FM20; Ripoche et al. 2020; Lee et al. 2021a, 2022; Parada et al. 2021, 2023; Zgirski et al. (2021; The Aracucaria Project, Z21)).

The JAGB method has several strengths when compared with the tip of the red giant branch (TRGB) and Leavitt law (Cepheid) distance indicators. First, with an intrinsic average magnitude of $M_J = -6.2$ mag, carbon stars are at least 1 mag brighter in the NIR than TRGB stars (which have an average intrinsic magnitude of $M_J \approx -5.1$ mag), thereby allowing farther distances to be probed. Second, only one epoch of observations is required to obtain a JAGB distance. Adding two to three epochs of data will significantly improve the precision of the JAGB measurement as discussed at the end of the section, but only one is necessary. On the other hand, more than a dozen epochs are needed to adequately measure the light curves (amplitudes, phases) and periods of Cepheids. Third, JAGB stars are found in all galaxies with stellar populations having ages between 200 Myr and 1 Gyr, whereas Cepheids can only be found in the young star-forming disks of dusty, gas-rich spiral and irregular galaxies. Fourth, JAGB stars are easily identified solely on the basis of their colors and magnitudes in the NIR. Fifth, JAGB stars are best observed in NIR observations, where the effects of reddening are significantly decreased compared with optical wavelengths.

A significant limitation of the JAGB method is, however, the small number of galaxies to which it has currently been applied, historically largely due to the limits of NIR facilities. Now, in this paper, we present high-precision *JHK* imaging of nearby galaxies to test and apply the JAGB method across a diverse sample of galaxies using imaging optimized for the carbon stars and analyzed homogeneously.

Furthermore, we measure NIR TRGB distances, a useful cross-checking tool for our JAGB distances, because any systematics affecting the JAGB method will be largely independent of those affecting the TRGB method in measuring distances. First, the JAGB method is based on an intermediate age and mass population of carbon-rich AGB stars (200 Myr–1 Gyr, 2–4.5 $M_\odot$), whereas RGB stars are significantly older and of lower mass (>4 Gyr, <2 $M_\odot$). The JAGB method (optimally) uses stars in the extended disks of galaxies, whereas the TRGB targets stars only in the less-crowded and low-reddening (dust-free) stellar halos. Finally, the astrophysical mechanisms by which these two methods are standard candles are completely independent; the JAGB method is based on the third dredge-up event for TP-AGB stars, and the TRGB is controlled by the explosive onset of helium burning in the cores of red giants. Therefore, any systematic related to any of these aforementioned characteristics (e.g., crowding, star formation history, metallicity) will affect the methods in independent ways. By comparing the two distances pairwise in the same galaxies, we can constrain these effects by sampling galaxies having a wide range of diverse star formation histories, metallicities, and dust environments.

This is the first study designed to provide a homogeneous sample for the purpose of measuring JAGB distances, where all galaxies have been observed with the same telescope/instrument and the data analyzed in a self-consistent manner. Previous studies that have calculated JAGB distances (which

[11] CO is the most strongly bonded molecule in the atmospheres of cool stars. Therefore, if all the O is already bound in CO, surplus C atoms are then available to form C_2 and CN. The high dissociation energy (11.1 eV) of carbon monoxide therefore profoundly affects the distinction in the spectra and observational properties between O-rich and C-rich AGB stars.

[12] Theoretical models predict that increased metallicity decreases the third dredge-up's efficiency and therefore the mass range of carbon star formation. For example, Pastorelli et al. (2020) found that at an initial metallicity of $Z_i = 0.004$ (the metallicity of the SMC), carbon stars formed at initial masses of $M_i \approx 1.4\ M_\odot$ to $M_i \approx 2.8\ M_\odot$, whereas at a higher metallicity of $Z_i = 0.008$ (the metallicity of the LMC), carbon stars formed at initial masses of $M_i \approx 1.7\ M_\odot$ to $M_i \approx 3.0\ M_\odot$. Because the initial mass of the star translates to its luminosity, the metallicity of the stellar environment would be theoretically expected to affect a population's average carbon star luminosity. On the other hand, *empirically*, Lee (2023) found zero metallicity dependence of the JAGB magnitude in the high-metallicity galaxy M31. However, further observational tests in a broader range of galaxy environments are needed to definitively constrain the JAGB method's dependence on metallicity.

Table 1
Galaxy Sample Properties (Ordered by Distance)

Galaxy	R.A. (J2000)	Decl. (J2000)	Morphological Type	A_J[a]	d (Mpc)[b]	Galaxy Group	JAGB LF Width (mag)[c]
NGC 6822	19 44 55	−14 48 00	Irregular	0.17	0.5	Local Group	0.30
IC 1613	01 04 48	+02 07 04	Irregular	0.02	0.8	Local Group	0.32
NGC 3109	10 03 09	−26 09 25	Spiral	0.05	1.2	Local Group	0.33
Sextans B	09 59 59	+05 20 20	Irregular	0.02	1.3	Local Group	0.30
Sextans A	10 11 01	−04 42 00	Irregular	0.03	1.4	Local Group	0.30
NGC 0300	00 54 54	−37 41 04	Spiral	0.01	1.8	Sculptor Group	0.32
NGC 0055	00 14 57	−39 11 48	Spiral	0.01	1.9	Sculptor Group	0.31
NGC 7793	23 57 50	−32 35 28	Spiral	0.01	3.1	Sculptor Group	0.35
NGC 247	00 47 09	−20 45 37	Spiral	0.01	3.2	Sculptor Group	0.32
NGC 5253	13 39 56	−31 38 24	Amorphous	0.04	3.3	Cen A/M83 Group	0.33
Cen A	13 25 28	−43 01 09	E/S0 (pec)	0.08	3.7	Cen A/M83 Group	⋯
NGC 1313	03 18 15	−66 29 50	Spiral	0.08	3.9	Isolated	0.36
M83	13 37 01	−29 51 57	Spiral	0.05	4.9	Cen A/M83 Group	⋯

Notes.
[a] Tabulated from NED: https://irsa.ipac.caltech.edu/applications/DUST/.
[b] The JAGB distances measured in this paper. For Cen A and M83, distances are from the EDD.
[c] Scatter on the mode $m_{\rm JAGB}$ for stars between $m_{\rm JAGB} \pm 0.75$ mag.

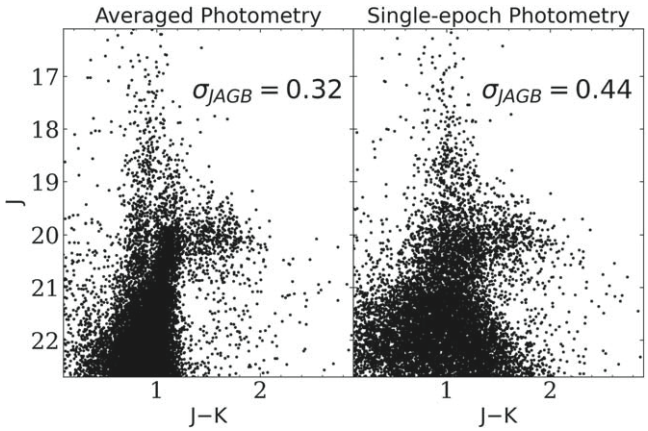

Figure 1. Example of how using time-averaged photometry decreases the measured scatter in the JAGB star LF. These two CMDs are of the galaxy NGC 300. On the left, we show photometry averaged from five nights of observing, and on the right, we show photometry from only one night of observing. The scatter shown in the upper right-hand corner was measured from the JAGB stars with magnitudes $m_J \pm 0.75$ mag, where m_J is the measured mode. The CMDs have the same stars.

were then compared with Cepheid or TRGB distances) to multiple galaxies were based on available published data (e.g., Freedman & Madore 2020; Z21; Parada et al. 2023). Differences in the photometry software, telescope, and sample selection of JAGB stars could have introduced additional scatter in comparisons between different distance indicators.

Furthermore, this study is idealized because we use multiepoch photometry to increase the precision of our measurements. Most JAGB stars are variable (Weinberg & Nikolaev 2001). The intrinsic variability of JAGB stars will thus contribute to the observed dispersion in the JAGB LF. The intrinsic scatter in the JAGB LF resulting from the variability of JAGB stars is ±0.2 mag (Madore & Freedman 2020a). Simply averaging two or more randomly observed epochs will bring down this scatter as $1/\sqrt{N_e}$, where N_e is the number of widely spaced epochs. For example, in Figure 1, we show two CMDs of NGC 300, one derived from one epoch of observing and one derived from three temporally averaged widely spaced epochs of observing (although these data encompass 5 total days—2011 September 9, 2011 October 5, 2011 November 3, 2021 September 17, and 2022 September 17—the data only span 3 total yr). The observed scatter (which includes the intrinsic scatter from the AGB stars' variability plus random scatter like photometric errors) measured from single-epoch data was 0.44 mag, whereas the scatter determined from temporally averaged photometry was measured to be 0.32 mag. This example demonstrates that JAGB measurements are more precise when derived from multiple epochs of data. Therefore, the data presented in this study are optimal for measuring high-precision JAGB distances.

The outline of this paper is as follows. In Section 2, we describe our Magellan FourStar observations and data reduction procedure. In Section 3, we describe the JAGB method and measured distances. In Section 4, we measure NIR TRGB distances to the galaxies in our sample. In Section 5, we compare our measured JAGB and TRGB distances with those from the literature. And finally, in Section 6, we summarize and conclude this paper.

2. Data

We obtained NIR *JHK* observations of the 13 galaxies at the 6.5 m Magellan–Baade telescope at Las Campanas Observatory with the wide-field FourStar NIR camera (Persson et al. 2013). The FourStar imager has a field of view of 10.′8 × 10.′8 and a plate scale of 0.″159 pixel^{-1}. The names and properties of these 13 galaxies are listed in Table 1. The FourStar images of the galaxies are shown in Figure 2. A log of our observations, which were taken from 2011 to 2023, can be found in Table 2. These observations were optimized for a study of JAGB stars in three ways.

1. For JAGB stars, only single-epoch photometry is needed to straightforwardly derive distances. However, by deriving mean photometry from multiple epochs, the intrinsic variability of the JAGB stars can be averaged over, thereby decreasing the dispersion in the observed LF. All of our galaxies have at least two observations in the J band.

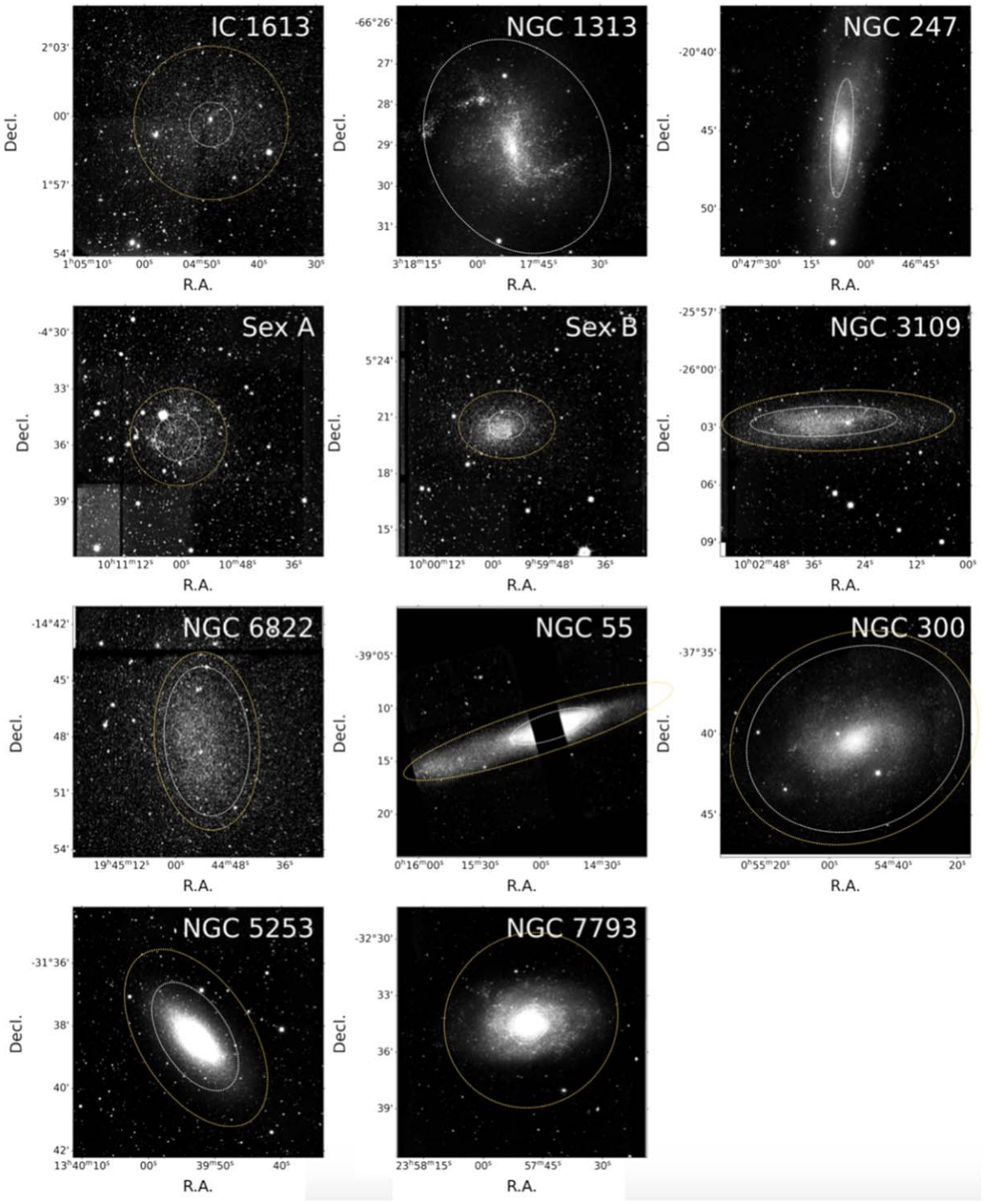

Figure 2. Images of the 11 galaxies observed with the FourStar camera on the 6.5 m Magellan–Baade telescope. The JAGB measurements were measured from all the data outside the dotted white ellipses, and the TRGB measurements were measured from all the data outside the dotted yellow ellipses.

Table 2
Observation Log

Galaxy	Date (yyyy mm dd)	Filter(s)
NGC 6822	2012 05 03	*JHK*
NGC 6822	2012 05 07	*JHK*
NGC 6822	2012 05 11	*JHK*
NGC 6822	2012 05 28	*JHK*
NGC 6822	2012 06 01	*K*

(This table is available in its entirety in machine-readable form.)

2. Our observations targeted the outer disks of galaxies, where reddening, crowding, and blending effects are minimized for the carbon stars.
3. All of these observations were taken with the same telescope, and photometry was extracted uniformly using the same suite of photometry software.

Photometry was extracted from the images using the DAOPHOT/ALLFRAME suite of photometry software (Stetson 1987). For a given galaxy, empirical point-spread functions were fit individually for each frame. A master source

Table 3
JAGB Method Systematic and Statistical Error Budget

Galaxy	Galactic Extinction (mag)	2MASS Phot. ZP (mag)	2MASS–FourStar Correction (mag)	Zero-point (mag)	Total σ_{sys} (mag)	Error on the Mode (mag)	Choice of σ_s (mag)	Zero-point (mag)	Total σ_{stat} (mag)
NGC 6822	0.09	0.01	0.01	0.04	0.10	0.02	0.05	0.01	0.05
IC 1613	0.01	0.01	0.01	0.04	0.04	0.04	0.09	0.01	0.10
NGC 3109	0.03	0.01	0.01	0.04	0.05	0.03	0.02	0.01	0.04
Sextans B	0.01	0.01	0.01	0.04	0.05	0.03	0.09	0.01	0.09
Sextans A	0.02	0.01	0.01	0.04	0.05	0.05	0.13	0.01	0.14
NGC 0300	0.01	0.01	0.02	0.04	0.05	0.02	0.02	0.01	0.03
NGC 0055	0.01	0.01	0.01	0.04	0.04	0.01	0.02	0.01	0.02
NGC 7793	0.01	0.01	0.02	0.04	0.05	0.01	0.10	0.01	0.10
NGC 247	0.01	0.01	0.01	0.04	0.04	0.01	0.02	0.01	0.02
NGC 5253	0.02	0.01	0.01	0.04	0.05	0.02	0.03	0.01	0.04
NGC 1313	0.04	0.01	0.01	0.04	0.06	0.01	0.02	0.01	0.03

Table 4
NIR TRGB Systematic and Statistical Error Budgets

Galaxy	Galactic Extinction (mag)	2MASS Phot. ZP (mag)	2MASS–FourStar Correction (mag)	Zero-point (mag)	Total σ_{sys} (mag)	Width of Edge Response (mag)	Zero-point (mag)	Total σ_{stat} (mag)
NGC 6822 (J)	0.09	0.01	0.01	0.06	0.11	0.002	0.01	0.01
NGC 6822 (H)	0.06	0.01	0.01	0.06	0.09	0.002	0.01	0.01
IC 1613 (J)	0.01	0.01	0.01	0.06	0.06	0.003	0.01	0.01
IC 1613 (H)	0.01	0.01	0.01	0.06	0.06	0.003	0.01	0.01
NGC 3109 (J)	0.05	0.01	0.01	0.06	0.08	0.005	0.01	0.01
NGC 3109 (H)	0.03	0.01	0.01	0.06	0.07	0.004	0.01	0.01
Sextans B (J)	0.02	0.01	0.02	0.06	0.07	0.005	0.01	0.01
Sextans B (H)	0.01	0.01	0.01	0.06	0.06	0.004	0.01	0.01
Sextans A (J)	0.03	0.01	0.01	0.06	0.07	0.007	0.01	0.01
Sextans A (H)	0.02	0.01	0.02	0.06	0.07	0.007	0.01	0.01
NGC 0300 (J)	0.01	0.01	0.02	0.06	0.06	0.002	0.01	0.01
NGC 0300 (H)	0.01	0.01	0.01	0.06	0.06	0.002	0.01	0.01
NGC 0055 (J)	0.01	0.01	0.01	0.06	0.06	0.003	0.01	0.01
NGC 0055 (H)	0.01	0.01	0.01	0.06	0.06	0.002	0.01	0.01
NGC 7793 (J)	0.01	0.01	0.02	0.06	0.07	0.004	0.01	0.01
NGC 5253 (J)	0.04	0.01	0.01	0.06	0.07	0.002	0.01	0.01

list was then constructed from an aligned and coadded image built from all of the individual images using MONTAGE2. We then photometered each of the individual frames simultaneously using the master source list.

Our final catalogs were cleaned using photometric quality cuts based on the J-band χ, sharp, and σ parameters of each star, following the procedure performed in Beaton et al. (2019) for the Carnegie–Chicago Hubble Program (CCHP). Photometric zero-points with respect to the Two Micron All Sky Survey (2MASS; Skrutskie et al. 2006) were derived by matching bright, unsaturated stars in our catalogs to 2MASS. We considered the following uncertainties associated with the photometric calibration in our error budget for both the JAGB method and TRGB (Tables 3 and 4, respectively): the 2MASS photometric zero-points (0.01 mag; Skrutskie et al. 2006) and the statistical uncertainty on the (2MASS–FourStar) transformation.

The deprojected galactocentric distance for every object in the catalogs was also calculated using the galaxy's position angle, inclination, and galactic center. These radial distances were then used to perform spatial cuts for the JAGB method (which optimally uses stars in the outer disk and halo) and TRGB method (which optimally uses stars in the halo). The spatial cuts used are shown in Figure 2.

All the final cleaned catalogs can be found on Zenodo at doi:10.5281/zenodo.10989065. Although the primary purpose of these observations was to measure JAGB distances, these catalogs could be used for other purposes. For example, these data could enable further studies on the NIR flux contribution of TP-AGB stars to the integrated luminosities of galaxies (e.g., Melbourne & Boyer 2013), reconstructing the star formation history of a galaxy from NIR data (e.g., Mazzi et al. 2021), tracing the age and metallicity gradients of galaxies using the C/M ratio of AGB stars (e.g., Cioni et al. 2008), and studying the red supergiant content of galaxies (e.g., Massey et al. 2021).

3. The JAGB Method

In this section, we determine JAGB method distances to the galaxies in our sample.

3.1. Measurement Procedure

JAGB stars are selected via their color to delineate them from oxygen-rich AGB stars on the blue side and extreme carbon stars on the red side. However, the exact colors used to select JAGB stars have varied inconsistently throughout the literature; in particular, the blue cutoff has ranged from $(J-K) > 1.3$ to 1.5. With our current homogeneous sample

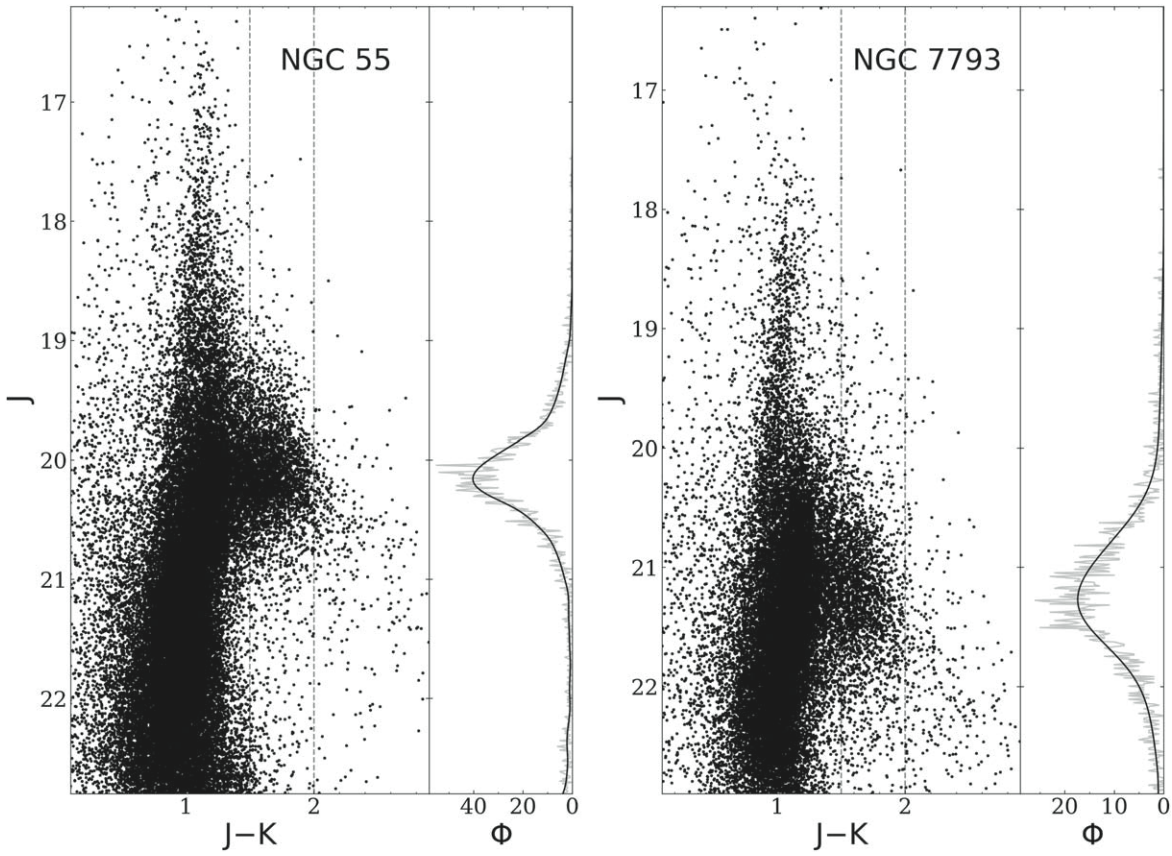

Figure 3. J vs. $(J-K)$ CMDs (left panels) and GLOESS-smoothed LFs in black overplotted on the binned LF in gray (right panels) for two example galaxies, NGC 55 and NGC 7793. The JAGB stars are located in the color range 1.5 mag $< (J-K) <$ 2.0 mag, between the dotted gray lines. The range of the y-axis is 6.6 mag for all the CMDs.

(The complete figure set (6 images) is available.)

of galaxies, we are now in a position to standardize the color range for selecting JAGB stars. Moving forward, we chose 1.5 mag $< (J-K) <$ 2.0 mag as the standard JAGB color cuts for every galaxy. The colors of carbon stars depend on the metallicity of the galaxy, where carbon stars have a bluer cutoff in low-metallicity environments. For example, Boyer et al. (2024) simulated carbon stars at two metallicities, $Z = 0.004$ and $Z = 0.014$, and found that the carbon stars at $Z = 0.004$ spanned approximately 1.3 mag $<$ (F090W − F150W) $<$ 4.5 mag in color, whereas the carbon stars at $Z = 0.014$ spanned approximately 1.8 mag $<$ (F090W − F150W) $<$ 4.5 mag in color. Therefore, by selecting carbon stars in a more conservative color range, we are prioritizing carbon star sample purity over completeness, particularly in the higher-metallicity galaxies. Furthermore, in Section 5, we found excellent agreement between the independent TRGB and JAGB distances, demonstrating that these chosen color cuts are effective for measuring accurate JAGB distances.

JAGB measurements are optimally performed in the outer disks of galaxies, where the JAGB stars are minimally affected by reddening, crowding, and blending (Lee et al. 2022). Therefore, first, we performed spatial cuts on our photometry, only using data in the outer disks. The spatial cuts are shown by the dotted white ellipses in Figure 2. Data inside these ellipses were excluded from the analysis.

Then, the JAGB stars were selected solely on the basis of their color, using color cuts of 1.5 mag $< (J-K) <$ 2.0 mag. Next, we generated the JAGB star LF by binning the J-band magnitudes of these stars using bins of 0.01 mag. We then smoothed the binned LF using a Gaussian-windowed, locally weighted scatterplot smoothing (GLOESS) algorithm, a data-smoothing interpolating technique that has been found to be effective at suppressing false, Poisson-noise-induced edges and peaks in LFs (Cleveland & Loader 1996; Loader 2004; Persson et al. 2004; Monson et al. 2017). The peak location of this LF marks the apparent JAGB magnitude. The only user input in this procedure is the smoothing parameter σ_s. We explore the systematics of the choice of σ_s later in Section 3.2. The CMDs and smoothed LFs for 11 of the galaxies are shown in Figure 3. Two galaxies, Cen A and M83 (the third-farthest and farthest galaxies in this sample, respectively), had significantly lower-quality CMDs and JAGB star LFs than the other 11 galaxies in our main sample. We discuss these two galaxies in Appendixes A.1 and A.2 and exclude them from the JAGB and TRGB analyses.

To measure the distance modulus to each galaxy, we used the JAGB zero-point from Madore et al. (2022b) of $M_J = -6.20 \pm 0.01$ (stat) $\pm$ 0.04 (sys) mag, which combines the geometric calibrations of the JAGB method from the LMC/SMC detached-eclipsing binaries (Madore & Freedman 2020a), Milky Way Gaia DR3 parallaxes (Lee et al. 2021b), and Milky Way open clusters (Madore et al. 2022b).

All of the apparent magnitudes were corrected for their line-of-sight foreground Galactic extinction, adopted from the

Schlegel et al. (1998) full-sky Galactic dust map recalibrated by Schlafly & Finkbeiner (2011).[13] These corrections are tabulated in Table 1. We adopted half of the galactic extinction value as its systematic uncertainty, per CCHP procedure (e.g., Beaton et al. 2019). Error budgets for each JAGB method measurement are shown in Table 3. The error on the mode of the smoothed LF was measured as $\sqrt{\Sigma(m_i - m_{\rm JAGB})^2}/N$, where $m_{\rm JAGB}$ is the mode, for stars with magnitudes $m_{\rm JAGB} \pm 0.5$ mag.

3.2. Effect of Smoothing Parameter Choice

To measure the effect of the choice of smoothing parameter σ_s, we varied the smoothing parameter from 0.15 mag to 0.45 mag in steps of 0.05 mag. We then adopted the largest change from the fiducial values listed in Table 3 as the statistical error due to the smoothing parameter choice, a procedure that was also utilized in Lee et al. (2022). For example, in NGC 300, the faintest mode was measured using smoothing parameters of $\sigma_s = 0.15$ mag and 0.20 mag: $m_{\rm JAGB} = 20.08$ mag. The brightest mode was measured using smoothing parameters of $\sigma_s = 0.30$, 0.35, 0.40, and 0.45 mag: $m_{\rm JAGB} = 20.06$ mag. For this galaxy, the fiducial mode of $m_{\rm JAGB} = 20.08$ mag was measured using a smoothing parameter of $\sigma_s = 0.20$ mag. The adopted statistical error due to the smoothing parameter for NGC 300 was then 0.02 mag.

However, robust statistical errors due to the effect of the smoothing parameter would be most accurately measured with a large sample of artificial stars. In the second paper of this series, we plan to show results for the effects of the smoothing parameter on the JAGB measurement error via artificial star tests. For now, however, we adopted these conservative statistical errors.

3.3. A Composite JAGB LF

Figure 4 shows a distance-corrected composite CMD of the 11 galaxies for which we measured JAGB distances. In this CMD, there are a total of ~6700 JAGB stars plotted $M_J \pm 0.5$ mag, where M_J was the measured mode of the composite JAGB star LF. The measured modal value was $M_J = -6.20 \pm 0.003$ (stat) mag. This JAGB star LF has a measured dispersion of 0.24 mag for stars with magnitudes of $M_J \pm 0.5$ mag. In Figure 4, we also show a red Gaussian fit to the binned LF overlaid on the black smoothed LF.

The composite JAGB star LF is symmetric and closely Gaussian in form. The 11 galaxies plotted here span a wide range of star formation histories, indicating that the underlying JAGB star LF of a (well-sampled) full star formation history is nearly perfectly symmetric and Gaussian.

4. NIR TRGB

The TRGB marks the onset of the helium flash for low-mass stars ($<2\ M_\odot$), when the star's degenerate helium core reaches a sufficiently high density and temperature of about 10^8 K via hydrogen shell fusion. At that point, the degeneracy of the core is lifted and the core reaches a hot enough temperature to begin helium burning (Salaris & Cassisi 1997). The star then settles onto the horizontal branch or red clump, depending on the initial mass and metallicity of the star.

[13] Determined from https://irsa.ipac.caltech.edu/applications/DUST/.

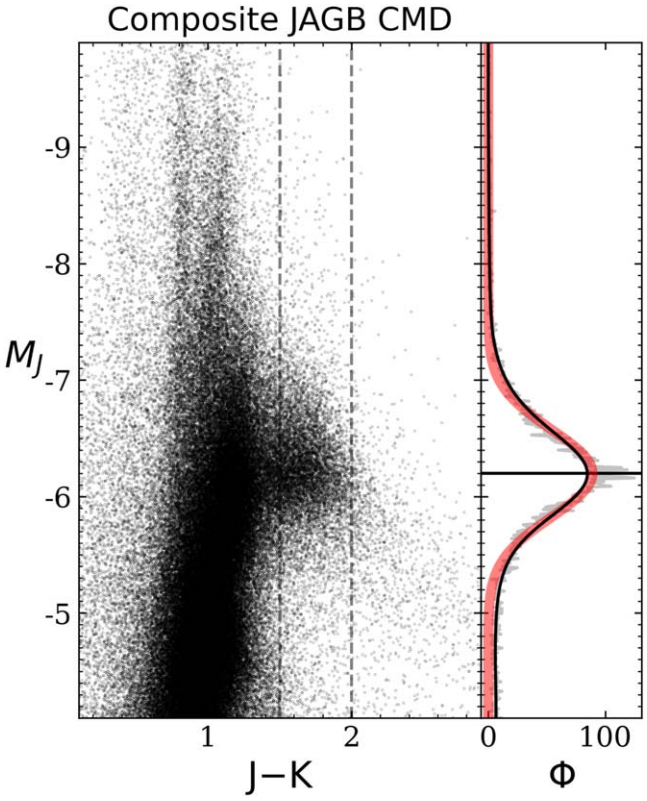

Figure 4. Composite distance-corrected CMD for the 11 galaxies with JAGB distances in this paper. The smoothed JAGB star LF is shown in black in the right panel, with a Gaussian fit in red overplotted. The black line marks the modal value at $M_J = -6.20 \pm 0.003$ mag.

In NIR wavelengths, the TRGB can be observed empirically as an upward-sloping discontinuity in a CMD of red giant branch (RGB) stars. The TRGB is brighter in the NIR than in the optical and therefore can probe farther distances than the more conventionally used *I*-band TRGB, which is flat with color (Hoyt et al. 2018; Madore et al. 2018; McQuinn et al. 2019; Freedman et al. 2020).

With our high-precision and well-sampled NIR data, we can also measure TRGB distances. To measure the NIR TRGB, we first performed spatial cuts on our data to exclude the disks of the galaxies, which have been shown to be problematic for TRGB measurements (e.g., Jang et al. 2021). It is imperative that the TRGB be measured in the stellar halos of galaxies, where there is less contamination from the younger AGB stars that may populate the region of color–magnitude space immediately above the TRGB. Furthermore, the effects of crowding and reddening are significantly diminished in the stellar halo. Our spatial cuts are shown in Figure 2 by the dotted yellow ellipses. Data inside the ellipse for each galaxy were removed.

Next, we selected the RGB stars using color cuts of $0.7 < (J - K) < 1.3$. Then, we employed the TRGB detection method first introduced by Madore et al. (2009). The data were transformed into *T*-band magnitudes, or "rectified," using slopes from Freedman et al. (2020; determined using LMC TRGB stars). The *T*-band magnitudes are designed to be insensitive to metallicity, thus leading the TRGB to be flat with color. For each galaxy, we constructed $T[J, (J - K)]$ and $T[H, (J - K)]$ magnitudes, excluding the *K* band because $m_J^{\rm TRGB}$ and $m_K^{\rm TRGB}$ are mathematically equivalent (see Madore &

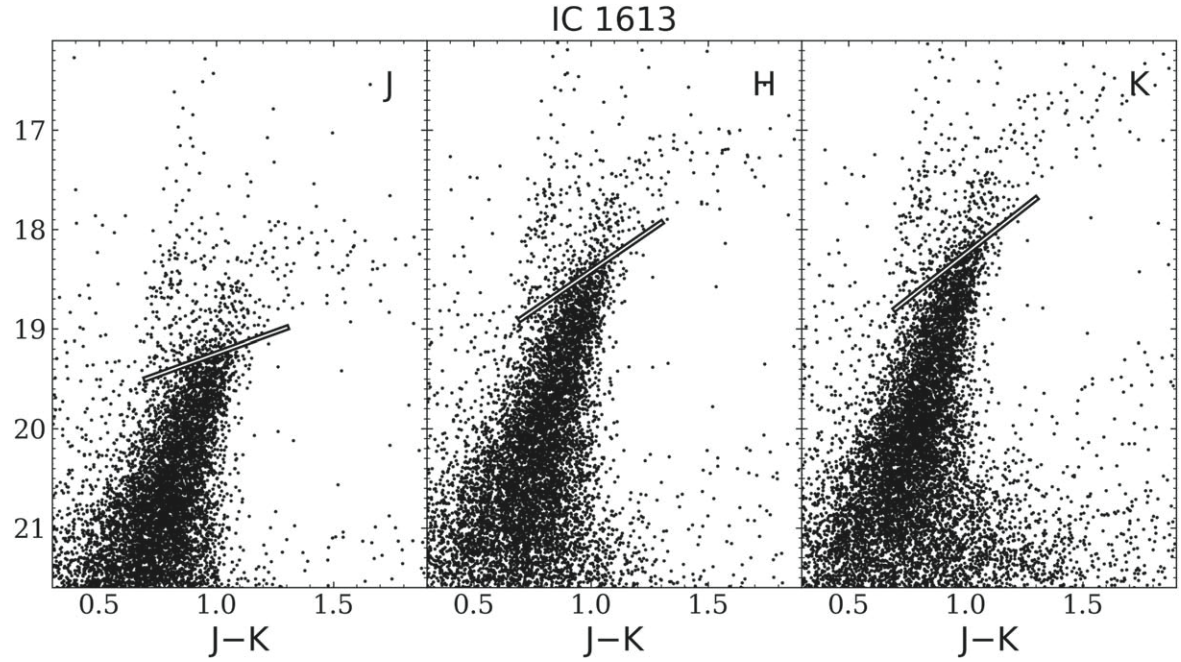

Figure 5. NIR CMDs for one example galaxy, IC 1613. The solid line shows the measured TRGB detection in the *J* and H bands. The TRGB was measured for stars with 0.7 mag $< (J-K) <$ 1.3 mag color, which is shown by the width of the solid line. The *J*-band TRGB was then projected into the *K* band and shown here in the right panel for each galaxy.

(The complete figure set (7 images) is available.)

Freedman 2020b). Then, the *T*-band RGB star LF for each band was constructed by finely binning the *T*-band magnitudes using bins of 0.01 mag. The *T*-band LFs were then smoothed using the GLOESS smoothing algorithm discussed in Section 3.1 using a smoothing parameter of $\sigma_s = 0.10$ mag. Smoothing filters have already been widely adopted in measuring the TRGB to suppress false edges in the LFs (due to noise). To measure the discontinuity in the *T*-band LF, we employed the method consistently used by the CCHP, introduced in Lee et al. (1993). First, the smoothed LF was convolved with a Sobel edge detection kernel [−1, 0, +1], resulting in a discrete approximation of the first derivative of the LF, i.e., the edge response function. The Sobel filter response was then weighted inversely by the Poisson noise calculated in the adjacent bins in the smoothed LF (described in Hatt et al. 2017). The maximum value of the edge response then marks the TRGB. Finally, we transformed the *T*-band TRGB values back into *J*- and *H*-band magnitudes to determine the final NIR TRGB intercepts. This rectification method has also been employed to measure the NIR TRGB in Madore et al. (2018), McQuinn et al. (2019), Cerny et al. (2020), Lee et al. (2022), and Parada et al. (2023, P23). The *T*-band LFs and edge detection response functions can be found in Appendix B. The *J*, *H*, and *K* versus $(J-K)$ CMDs and TRGB measurements are shown in Figure 5.

Madore et al. (2009) showed that with at least 400 stars below the TRGB, the tip could be measured to within ∼0.1 mag at the 85% confidence level. Then, in a recently updated paper on simulations of TRGB detections across a range of smoothing parameters, photometric errors, and number of RGB stars, Madore et al. (2023) found that "one should not even attempt a tip detection at low signal-to-noise in situations where the [TRGB] population size is only in the hundreds. Spurious signals will be found above and below the true tip." In particular, for a population of 120 RGB stars with average photometric errors of ±0.05 mag and a smoothing parameter of $\sigma_s = 0.10$ mag, wild statistical fluctuations in both the LF and edge response function led to false-positive detections ±1 mag above and below the TRGB. Therefore, we have only measured TRGB distances to galaxies in our sample that have ample TRGB halo stars. NGC 1313 and NGC 247 did not have deep enough data to do any TRGB measurement and so were excluded entirely. NGC 7793 did not have deep enough *H*-band data, and NGC 5253 lacked *H*-band data, so these galaxies only have *J*-band TRGB measurements. We also note that Madore et al. (2023) found that for 1200 stars in the RGB that had photometric errors of ±0.05 mag and a LF smoothed with a smoothing parameter of $\sigma_s = 0.10$ mag, the tip detection was found to be accurate to ±0.03 mag. We confirmed that the photometric errors of the RGB stars at ±0.2 mag of the TRGB in this sample were typically ±0.03 to ±0.05 mag.

We determined distance moduli based on the absolute calibrations from Hoyt et al. (2018), which we repeat below. The errors on these zero-points are ±0.01 (stat) and ±0.06 (sys) mag:

$$M_J^{\rm TRGB} = -5.14 - 0.85 \times [(J-K)_o - 1.00], \quad (1)$$

$$M_H^{\rm TRGB} = -5.94 - 1.62 \times [(J-K)_o - 1.00]. \quad (2)$$

In Table 4, we tabulate all the uncertainties for each TRGB distance. This includes a statistical uncertainty derived from the width of the *T*-band LF edge response divided by the square root of the number of stars contributing to the response at that magnitude (Beaton et al. 2019). As in Section 3, we also applied galactic extinction corrections to the apparent magnitudes and adopted half of the extinction value as its systematic uncertainty. In Table 5, we also list the final

Table 5
Measured JAGB and TRGB Apparent Magnitudes and Relevant Foreground Extinctions

Galaxy	$m^{\rm JAGB}$	$m_J^{\rm TRGB}$	$m_H^{\rm TRGB}$	A_J	A_H
NGC 6822	17.54	18.65	17.83	0.17	0.11
IC 1613	18.27	19.25	18.42	0.02	0.01
NGC 3109	19.31	20.40	19.54	0.05	0.03
Sextans B	19.32	20.50	19.70	0.02	0.01
Sextans A	19.54	20.66	19.83	0.03	0.02
NGC 0300	20.08	21.13	20.38	0.01	0.01
NGC 0055	20.16	21.24	20.54	0.01	0.01
NGC 7793	21.27	22.31	⋯	0.01	⋯
NGC 0247	21.35	⋯	⋯	0.01	⋯
NGC 5253	21.44	22.61	⋯	0.04	⋯
NGC 1313	21.83	⋯	⋯	0.08	⋯

measured TRGB values and extinction corrections for each galaxy. Finally, in Figure 6, we show a composite distance-corrected CMD of the nine galaxies with TRGB distances in this paper.

5. Distance Comparisons

In Figure 7, we show a TRGB–JAGB comparison of the distances for the nine galaxies in this sample that have both measured JAGB and TRGB distances, along with our distances measured to WLM (Lee et al. 2021a) and M33 (Lee et al. 2022) in companion papers. The mean offset between all the measured distances was measured to be $<\mathrm{TRGB}-\mathrm{JAGB}>=+0.036\pm0.021$ mag (standard error on the mean). The 11 galaxies in Figure 7 have an rms scatter about a unit-slope line of ±0.07 mag. If we attribute this scatter equally to both methods (meaning $0.07^2=\sigma^2_{\rm JAGB}+\sigma^2_{\rm TRGB}$), this then suggests that each of the two methods can individually measure distances with 2% precision for nearby galaxies. Alternatively, by assuming that the scatter results entirely from the JAGB method, this comparison suggests that JAGB distances would still be individually measured with 3% precision.

Two other studies have undertaken similar TRGB–JAGB comparisons; Freedman & Madore (2020) and Madore et al. (2022a) both measured an rms scatter of ±0.08 mag. The Araucaria Project (Z21) also compared JAGB–Cepheid distances between seven galaxies, finding an rms scatter of ±0.09 mag. However, all these observations originally targeted populations other than the JAGB stars (often Cepheids) and were not analyzed homogeneously using data from the same telescope. In comparison, all our TRGB and JAGB distances were derived from the same imaging and used photometry averaged over multiple epochs, designed to beat down the scatter introduced by the variability of the JAGB stars. Furthermore, we performed spatial cuts to exclude the crowded inner disks of galaxies.

As discussed in the Introduction, the TRGB and JAGB are drawn from entirely separate stellar populations and therefore will likely have completely unrelated astrophysical systematics. The observed scatter of ±0.07 mag from the TRGB–JAGB comparison includes all the cumulative effects of differences potentially resulting from host galaxy types, metallicities, star formation histories, and uncorrected reddening effects. That is, all systematics are constrained in each distance indicator at the ±0.05 mag (2% in distance) level or less.

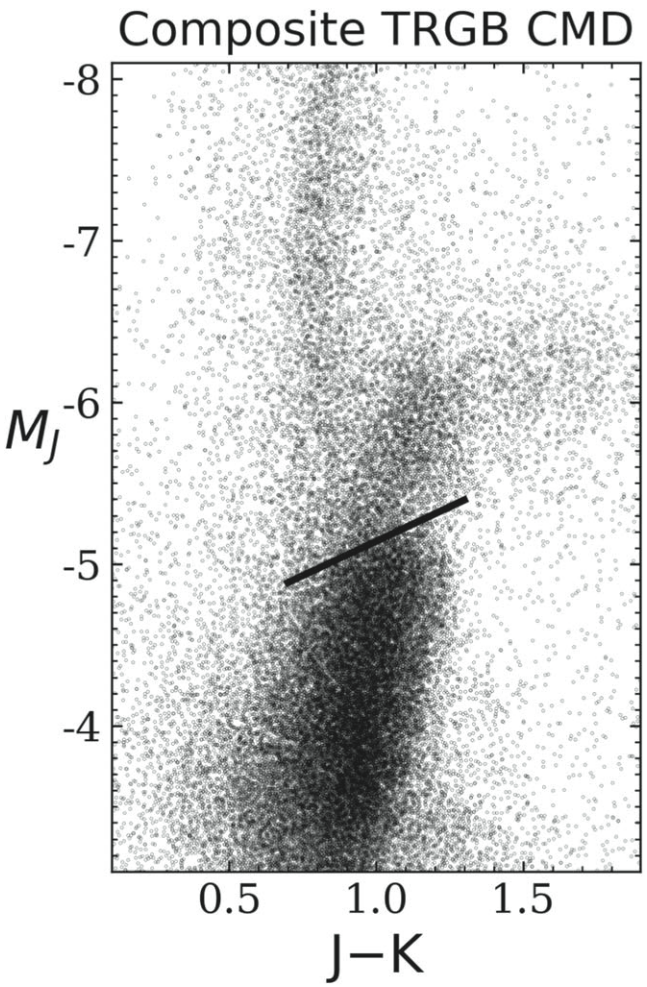

Figure 6. Composite distance-corrected CMD for the nine galaxies with TRGB distances in this paper. The black line denotes the *J*-band TRGB.

5.1. Comparisons with JAGB Distances from the Literature

In this section, we compare our measured JAGB distance moduli to JAGB distances reported in the literature.

In Table 6, we have compiled all available NIR TRGB and JAGB distance moduli to the galaxies in our sample. A visual representation of this table is also shown in Figure 8. We also tabulated *I*-band TRGB distance moduli from the following sources. IC 1613 has had its *I*-band TRGB distance measured by the CCHP, which we listed; for the rest of the galaxies, we recorded *I*-band TRGB distances from the Extragalactic Distance Database (EDD; Jacobs et al. (2009; EDD, J09); Tully et al. 2009; Anand et al. 2021) and the ACS Nearby Galaxy Survey Treasury (ANGST; Dalcanton et al. (2009; ANGST, D09)). To avoid redundancy, if the EDD distance was based on observations collected for ANGST, we exclusively recorded the ANGST distance. We have also tabulated the two Cepheid distances from the Carnegie Hubble Program (CHP), the predecessor to the CCHP. The CHP utilized the FourStar *JHK* photometry from this paper (taken previous to 2012) and Spitzer [3.6]- and [4.5]-band photometry to measure multi-wavelength Leavitt law distances to NGC 6822 (Rich et al. 2014) and IC 1613 (Scowcroft et al. 2013).

In the following subsections, we discuss how our JAGB distances compare with those from the literature. For galaxies that have yet to have their distances measured with the JAGB

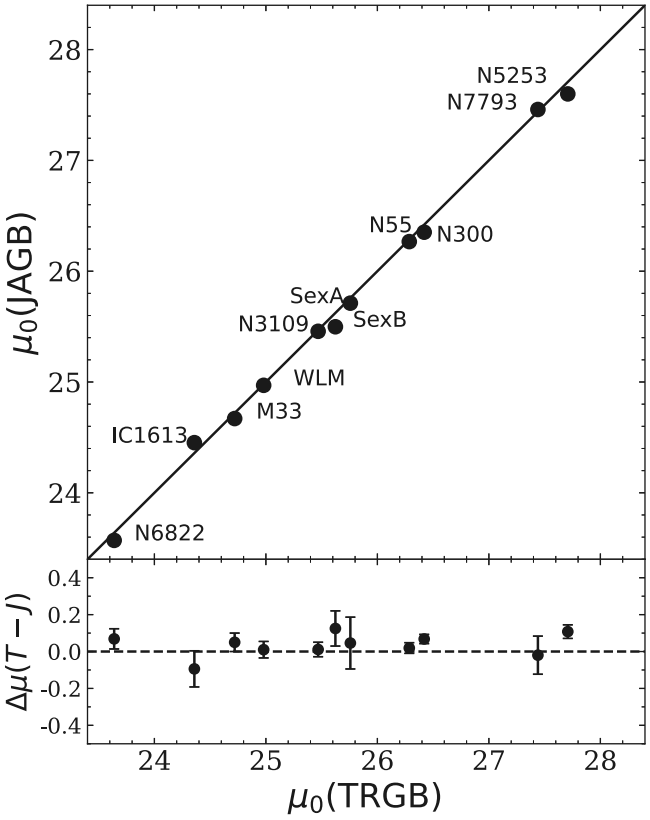

Figure 7. Comparison of 11 TRGB and JAGB distance moduli. The diagonal black line is not a fit to the data but a line of slope 1, showing the excellent agreement between the TRGB and JAGB methods. The 1σ scatter measured about the unit-slope black line is ± 0.07 mag. The distances span a range from about 0.5 to 3.3 Mpc. The bottom panel shows the difference between the distance moduli (TRGB minus JAGB distance modulus) as a function of the TRGB distance modulus. The error bars represent the statistical TRGB and JAGB errors added in quadrature.

method before this paper (Sextans B, Sextans A, NGC 5253, and NGC 1313), we instead cross-checked with literature distances from the *I*-band TRGB. In the cases where our JAGB distances significantly disagreed with the *I*-band TRGB distances (Sextans B and NGC 1313), we further cross-compared with distances derived from Cepheid stars. We discuss the galaxies in three subsections: Sections 5.1.1, 5.1.2, and 5.1.3 discuss galaxies whose JAGB distances agree well with those from the literature, disagree with literature results, and have mixed agreement with the literature, respectively.

We also hereafter refer to the following papers by the following initialisms: FM20, P23, Z21, J09, and D09. In particular, FM20, P23, and Z21 all measured multiple JAGB distances, and J09 and D09 measured *I*-band TRGB distances for a large sample of galaxies. P23 also measured multiple NIR TRGB distances.

5.1.1. Galaxies with Good Literature Agreement: IC 1613, Sextans A, NGC 55, and NGC 5253

IC 1613. IC 1613's low foreground and internal extinction should make it an easy target for measuring distances, so it is reassuring that our JAGB measurement agrees with those from the literature to within 1σ. Our JAGB distance also agrees at the 1.4σ level with the CHP multiwavelength Leavitt law distance from Scowcroft et al. (2013), which utilized the same *JHK* imaging from this paper (taken in 2011) as well as Spitzer [3.6]- and [4.5]-band photometry.

Sextans A. There are no JAGB distances to Sextans A available in the literature, so we instead compared our measured JAGB distance to *I*-band TRGB distances from ANGST. Our JAGB distance modulus agrees to within 1σ with the ANGST *I*-band TRGB measurement.

NGC 55. Our measured JAGB distance agrees almost exactly with the JAGB distance modulus measured by P23.

NGC 5253. There are no JAGB distances to NGC 5253 available in the literature, so we instead compared our measured distance to *I*-band TRGB distances from the EDD. Our JAGB measurement agrees to within 1σ with the EDD *I*-band TRGB measurement.

5.1.2. Galaxies with Poor Literature Agreement: Sextans B, NGC 7793, and NGC 1313

Sextans B. There are no JAGB distances to Sextans B available in the literature, so we instead compared our measured distances to *I*-band TRGB distances from ANGST and EDD. Our JAGB measurement is in more than 2σ tension with the ANGST and EDD *I*-band TRGB measurements. One potential explanation is that ANGST and EDD both used disk fields for their TRGB measurements, which would lower the precision and accuracy of their detection of the TRGB. As an additional cross-check, we also compare our JAGB distance with the only recent Cepheid measurement to Sextans B in the literature from Tammann et al. (2011) of $\mu_0 = 25.53 \pm 0.10$ mag, which agrees well with our JAGB distance modulus.

NGC 7793. Our JAGB distance modulus disagrees at the 2.1σ level with the Z21 JAGB measurement. We note that the field used by Z21 for their analysis contains the nucleus of NGC 7793. Reddening effects from the inner disk of this galaxy may explain why the Z21 measurement is 0.24 mag fainter than our JAGB measurement. Furthermore, Z21 used a larger reddening correction of 0.07 mag (derived from Cepheids), compared with our correction of 0.01 mag (the foreground extinction value from Schlegel et al. 1998). If we used the same reddening correction, this would bring our measurements into 1.6σ agreement.

NGC 247. Our JAGB distance disagrees with Z21 by 2.4σ. This difference can be straightforwardly attributed to our differing reddening corrections. Z21 used an extinction correction of $A_J = 0.16$ mag, derived from Cepheids, compared to our foreground reddening value of $A_J = 0.01$ mag. Our measured uncorrected JAGB magnitudes agree to within 0.02 mag.

NGC 1313. There are no JAGB distances to NGC 1313 available in the literature, so we instead compared our measured distance to *I*-band TRGB distances from the EDD. Our JAGB measurement disagrees with the EDD *I*-band TRGB measurement by 2.8σ. There are a couple of potential explanations for this discrepancy. First, the EDD *I*-band TRGB measurement was made in the outer disk of NGC 1313, and there seems to be a significant number of AGB stars blurring the tip measurement.[14] Second, at 3.9 Mpc away, NGC 1313 is 0.6 Mpc farther than NGC 5253, the second-farthest galaxy in this sample. As a cross-check, only one Cepheid distance measurement has been made to NGC 1313: $\mu_0 = 28.31 \pm 0.10$ mag (Qing et al. 2015), which disagrees with both our JAGB distance modulus and the

[14] https://edd.ifa.hawaii.edu/get_cmd.php?pgc=12286

Table 6
Literature Distances

Galaxy	Method	μ_0	Reference	Notes
NGC 6822	*I*-band TRGB	23.62 ± 0.08	J09	$m_{F814W} = 19.97 \pm 0.07$ mag, $A_{F814W} = 0.40$ mag
NGC 6822	NIR TRGB	23.39 ± 0.02	P23	*K*-band TRGB
NGC 6822	NIR TRGB	23.64 ± 0.10	This study	
NGC 6822	Leavitt law	23.38 ± 0.04	CHP (Rich et al. 2014)	
NGC 6822	JAGB method	23.44 ± 0.02	FM20	
NGC 6822	JAGB method	23.24 ± 0.04	Z21	
NGC 6822	JAGB method	23.52 ± 0.03	P23	
NGC 6822	JAGB method	23.57 ± 0.11	This study	
IC 1613	*I*-band TRGB	24.40 ± 0.04	Hatt et al. (2017)	$m_{F814W} = 20.35 \pm 0.01$ mag, assumed zero Galactic extinction
IC 1613	NIR TRGB	24.32 ± 0.05	Madore et al. (2018)	
IC 1613	NIR TRGB	24.45 ± 0.03	P23	*K*-band TRGB
IC 1613	NIR TRGB	24.36 ± 0.06	This study	
IC 1613	Leavitt law	24.29 ± 0.04	CHP (Scowcroft et al. 2013)	
IC 1613	JAGB method	24.36 ± 0.05	FM20	$m_J = -6.20 \pm 0.04$ mag
IC 1613	JAGB method	24.46 ± 0.05	P23	
IC 1613	JAGB method	24.45 ± 0.11	This study	
NGC 3109	*I*-band TRGB	25.64 ± 0.10	J09	$m_{F814W} = 21.69 \pm 0.09$ mag, $A_{F814W} = 0.10$ mag
NGC 3109	*I*-band TRGB	25.60 ± 0.04	D09	Two fields, $m_{F814W} = 21.65 \pm 0.02$ mag, $A_{F814W} = 0.10$ mag
NGC 3109	NIR TRGB	25.58 ± 0.04	P23	*K*-band TRGB
NGC 3109	NIR TRGB	25.47 ± 0.08	This study	
NGC 3109	JAGB method	25.52 ± 0.05	Z21	
NGC 3109	JAGB method	25.59 ± 0.03	P23	
NGC 3109	JAGB method	25.56 ± 0.05	FM20	
NGC 3109	JAGB method	25.46 ± 0.06	This study	
Sextans B	*I*-band TRGB	25.80 ± 0.05	J09	$m_{F814W} = 21.80 \pm 0.03$ mag, $A_{F814W} = 0.05$ mag
Sextans B	*I*-band TRGB	25.82 ± 0.04	D09	$m_{F814W} = 21.82 \pm 0.02$ mag, $A_{F814W} = 0.05$ mag
Sextans B	NIR TRGB	25.62 ± 0.07	This study	
Sextans B	JAGB method	25.50 ± 0.10	This study	
Sextans A	*I*-band TRGB	25.82 ± 0.05	D09	$m_{F814W} = 21.84 \pm 0.03$ mag, $A_{F814W} = 0.07$ mag
Sextans A	NIR TRGB	25.76 ± 0.07	This study	
Sextans A	JAGB method	25.71 ± 0.15	This study	
NGC 0300	*I*-band TRGB	26.51 ± 0.04	D09	Six fields, $m_{F814W} = 22.48 \pm 0.02$ mag, $A_{F814W} = 0.02$ mag
NGC 0300	NIR TRGB	26.29 ± 0.06	This study	
NGC 0300	JAGB method	26.30 ± 0.02	Madore et al. (2022a)	Median JAGB magnitude
NGC 0300	JAGB method	26.47 ± 0.06	Z21	
NGC 0300	JAGB method	26.27 ± 0.05	This study	
NGC 0055	*I*-band TRGB	26.66 ± 0.04	D09	Four fields, $m_{F814W} = 22.63 \pm 0.01$ mag, $A_{F814W} = 0.02$ mag
NGC 0055	*I*-band TRGB	26.69 ± 0.05	J09	$m_{F814W} = 22.66 \pm 0.03$ mag, $A_{F814W} = 0.02$ mag
NGC 0055	NIR TRGB	26.42 ± 0.06	This study	
NGC 0055	JAGB method	26.36 ± 0.02	Z21	
NGC 0055	JAGB method	26.35 ± 0.05	This study	
NGC 7793	*I*-band TRGB	27.78 ± 0.07	J09	$m_{F814W} = 23.76 \pm 0.06$ mag, $A_{F814W} = 0.03$ mag
NGC 7793	NIR TRGB	27.44 ± 0.07	This study	
NGC 7793	JAGB method	27.70 ± 0.03	Z21	
NGC 7793	JAGB method	27.46 ± 0.11	This study	
NGC 0247	*I*-band TRGB	27.76 ± 0.06	D09	Two fields, $m_{F814W} = 23.74 \pm 0.04$ mag, $A_{F814W} = 0.03$ mag
NGC 0247	JAGB method	27.41 ± 0.02	Z21	
NGC 0247	JAGB method	27.54 ± 0.05	This study	
NGC 5253	*I*-band TRGB	27.65 ± 0.04	J09	$m_{F814W} = 23.69 \pm 0.02$ mag, $A_{F814W} = 0.09$ mag
NGC 5253	NIR TRGB	27.71 ± 0.07	This study	
NGC 5253	JAGB method	27.60 ± 0.06	This study	
NGC 1313	*I*-band TRGB	28.17 ± 0.05	J09	$m_{F814W} = 24.29 \pm 0.03$ mag, $A_{F814W} = 0.17$ mag
NGC 1313	JAGB method	27.95 ± 0.06	This study	

Note. All *I*-band TRGB distance moduli have been standardized to use the Freedman (2021) zero-point of $M_{F814W} = -4.05 \pm 0.04$ mag. If there were multiple TRGB measurements from different fields in the same paper, we took the average.

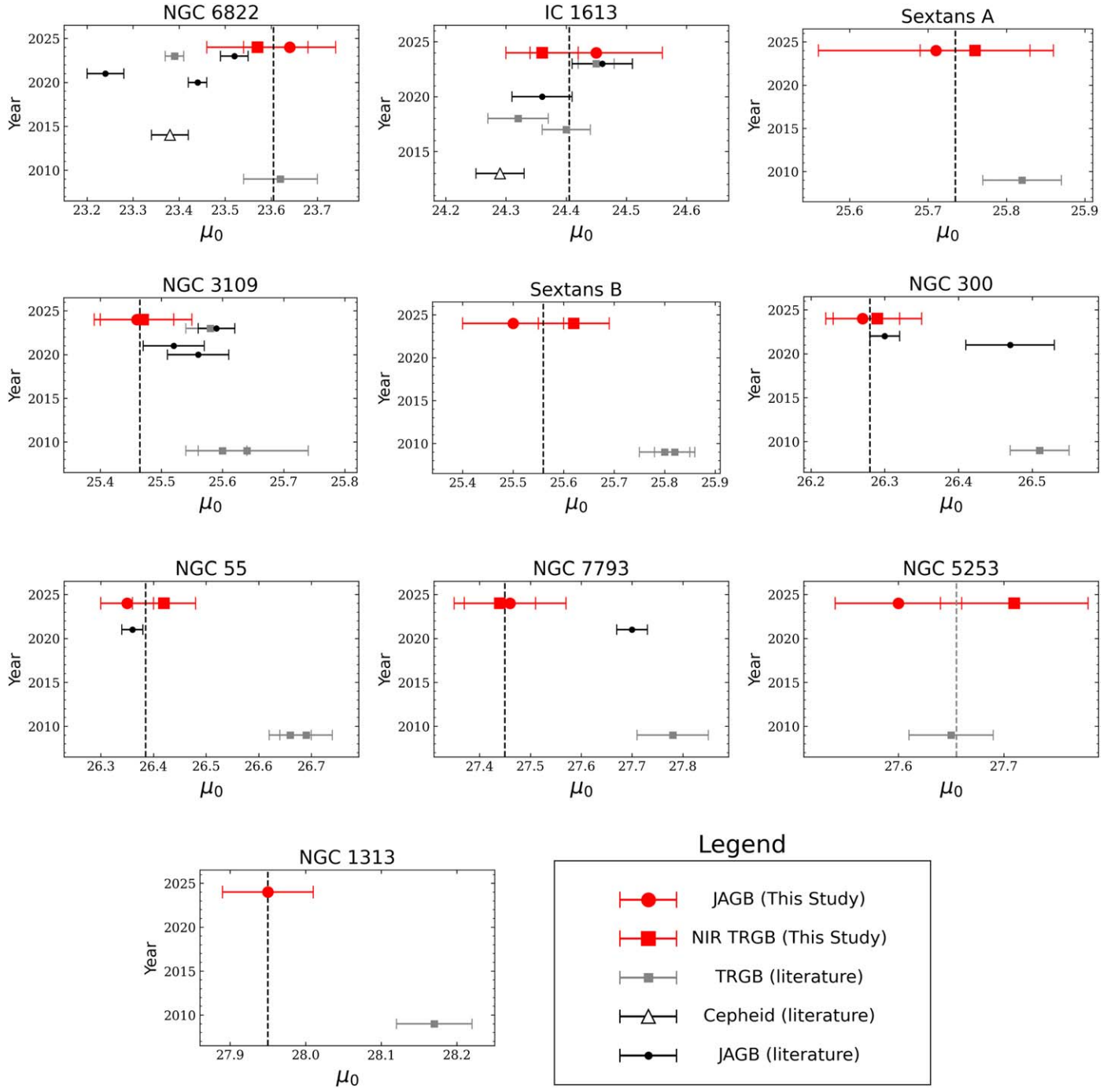

Figure 8. A visual representation of Table 6, showing comparisons between our measured JAGB and NIR TRGB distances with those from the literature, ordered by year, for each galaxy. For distances from the literature: gray squares represent TRGB measurements, black circles represent JAGB measurements, and white triangles represent CHP Cepheid measurements. Red squares and red circles represent the TRGB and JAGB distances measured in this study, respectively. The dotted black line marks the average of the measured JAGB and TRGB distance moduli from this study.

EDD *I*-band TRGB distance modulus significantly. Therefore, it is possible that NGC 1313 is at the distance where it is difficult to measure accurate JAGB method distances with ground-based NIR telescopes.

5.1.3. Galaxies with Mixed Literature Agreement: NGC 6822, NGC 3109, and NGC 300

NGC 6822. Our JAGB distance modulus agrees to within $\sim 1\sigma$ with the JAGB distance moduli from FM20 and P23. However, our measurement disagrees at the 2.8σ level with the Z21 measurement. Some of this disagreement results from the different reddening corrections used; we used a foreground correction of $A_J = 0.17$ mag, while Z21 used $A_J = 0.31$ mag, which was derived from a reddening law fit for the Cepheid P-L relations in NGC 6822. If Z21 used our reddening correction instead, our JAGB distance moduli agree at the 1.6σ level. Next, we note that Z21 averaged their JAGB measurement from two separate data sets. The first data set, from the SOFI camera on the New Technology Telescope, yielded a distance modulus of $\mu_0 = 23.19 \pm 0.04$ mag, and the

second data set, from the PANIC instrument (the predecessor to the FourStar Camera) on the Magellan–Baade telescope, yielded $\mu_0 = 23.30 \pm 0.04$ mag. Therefore, the two independent data sets produce JAGB magnitudes that disagree by 0.11 mag. Thus, the disagreement between our JAGB magnitude versus the Z21 JAGB magnitude may have resulted from a systematic photometric offset difference between our catalogs. As an additional cross-check, we also compared our JAGB distance with the CHP multiwavelength Leavitt law distance from Rich et al. (2014), which utilized the same *JHK* imaging from this paper (taken in 2012 May) as well as Spitzer [3.6]- and [4.5]-band photometry. Our JAGB distances agrees at the 1.6σ level with this Cepheid distance.

NGC 3109. Our JAGB distance to NGC 3109 agrees to within 1.3σ with Z21 and FM20. However, our JAGB measurement disagrees at the 1.9σ level with the JAGB distance from P23. This disagreement could potentially be because P23 performed their JAGB measurement in the inner disk of NGC 3109, where reddening effects could bias their result fainter.

NGC 300. Our JAGB distance agrees well with that from Madore et al. (2022a), who used the Hubble Space Telescope WFC3/IR F110W filter to measure a distance modulus to NGC 300. On the other hand, our JAGB measurement disagrees to about 2.5σ with the Z21 Araucaria project JAGB measurement. Some of this disagreement can be straightforwardly attributed to our different reddening corrections. Z21 used a reddening correction of $A_J = 0.08$ mag derived from Cepheids compared with our correction of $A_J = 0.01$ mag; using the same correction brings our measurements into 1.7σ agreement. Furthermore, the fields used by Z21 encompass the inner disk of NGC 300, where reddening could be biasing their result fainter.

5.1.4. Summary

In summary, most differences between our JAGB measurements and those from the literature can be straightforwardly attributed to differing reddening corrections. Accounting for these differences, we overall find excellent agreement ($\lesssim 1.5\sigma$) between our JAGB distances and those from the literature, with the exception of NGC 3109 and NGC 300. However, we speculate that the choice of field (inner disk versus outer disk) and the resulting reddening bias incurred may potentially explain these differences.

6. Conclusion

In this paper, we have created a repository of NIR stellar photometry for nearby galaxies ($d < 4$ Mpc). This photometry was temporally averaged from multiple-epoch observations, designed to decrease the dispersion in the observed JAGB star LF. The resulting catalogs will be useful for comprehensive studies of nearby stellar populations in the NIR.

The method used in this paper for measuring the apparent JAGB magnitude via the modal magnitude of the GLOESS-smoothed LF (after selecting JAGB stars in the color region $1.5 \text{ mag} < (J-K) < 2.0$ mag) was shown to be robust. The residuals obtained from subtracting the JAGB distance moduli from the TRGB distance moduli yielded an rms scatter of $\sigma = 0.07$ mag. For this sample of galaxies, this scatter puts upper limits (<2%) on the impact of metallicity differences, internal reddening, and star formation history differences between galaxies on the JAGB method distances. Furthermore, we showed that the composite JAGB star LF formed from the diverse sample of galaxies is closely Gaussian in form. This demonstrates that the underlying JAGB star distribution of a complete star formation history is Gaussian and symmetric.

Further work should quantify directly how distances measuring using the JAGB method are affected by astrophysical systematics. For example, Lee (2023) showed that metallicity and age were not significantly correlated with the mode of the JAGB star LF in M31. However, M31 is a relatively metal-rich galaxy. Extending this analysis to a wider range of environments will help further quantify the effects of metallicity and star formation history on the JAGB star LF. Furthermore, we plan to simulate artificial star tests for several galaxies in this sample, which will allow us to more accurately quantify the effects of the choice of smoothing parameter on the JAGB star LF.

With this further development and testing, the JAGB method has significant potential to provide an independent calibration of Type Ia supernovae with JWST and therefore a measurement of the Hubble constant.

Acknowledgments

We gratefully acknowledge the efforts and dedication of the Las Campanas Observatory staff for support, particularly in remote observing during the COVID-19 pandemic. In particular, we thank Jorge Araya, Carlos Contreras, Matías Díaz, and Carla Fuentes. We also want to especially thank Eric Persson, who created, built, and supported FourStar over many years and without whom this project never would have come to fruition. A.J.L. thanks Saurabh Jha for helpful comments on error budgets. We thank Peter Stetson for providing us with a copy of DAOPHOT and continually helping us troubleshoot problems. We thank Taylor Hoyt for his TRGB measurement code. Finally, we thank the anonymous referee for the constructive and helpful suggestions that improved this work.

A.J.L. was supported by the Future Investigators in NASA Earth and Space Science and Technology (FINESST) award No. 80NSSC22K1602 during the completion of this work. A.J.L. thanks the LSSTC Data Science Fellowship Program, which is funded by LSSTC, NSF Cybertraining grant No. 1829740, the Brinson Foundation, and the Moore Foundation; her participation in the program has benefited this work. Finally, we thank the Observatories of the Carnegie Institution for Science and the University of Chicago for their support of our long-term research into the calibration and determination of the expansion rate of the Universe.

This paper is based on data obtained using the FourStar infrared imager on the 6.5 m Magellan Telescopes located at Las Campanas Observatory, Chile. This research has made use of the NASA/IPAC infrared Science Archive (IRSA), which is operated by the Jet Propulsion Laboratory, California Institute of Technology, under contract with the National Aeronautics and Space Administration. This publication makes use of data products from the Two Micron All Sky Survey, which is a joint project of the University of Massachusetts and the Infrared Processing and Analysis Center/California Institute of Technology, funded by the National Aeronautics and Space Administration and the National Science Foundation. This research has made use of NASA's Astrophysics Data System Bibliographic Services.

The data are available on Zenodo under an open-source Creative Commons Attribution license: doi:10.5281/zenodo.10989065.

Facility: Magellan:Baade (FourStar).

Software: DAOPHOT (Stetson 1987), Astropy (Astropy Collaboration et al. 2013, 2018, 2022), Matplotlib (Hunter 2007), NumPy (Harris et al. 2020), Pandas (McKinney 2010), scipy (Virtanen et al. 2020).

Appendix A
Anomalous Galaxies

We were unable to measure precise distances to two galaxies in our sample, M83 and Cen A. As shown in Figure A1, neither of the JAGB star LFs for these galaxies has a clearly defined peak location. In Appendixes A.1 and A.2, we speculate on potential explanations for our difficulties in measuring precise distances to these galaxies. The images of both galaxies are shown in Figure A2.

A.1. Cen A

Cen A (NGC 5128) has a notoriously complex star formation history, as well as radio jets, dust lanes, and X-ray sources. Its morphological type, either an elliptical galaxy with a prominent dust lane or a peculiar S0, has been a source of debate in the literature (Harris 2010). As shown in Table A1, recent distances in the literature to Cen A range from the Cepheid-

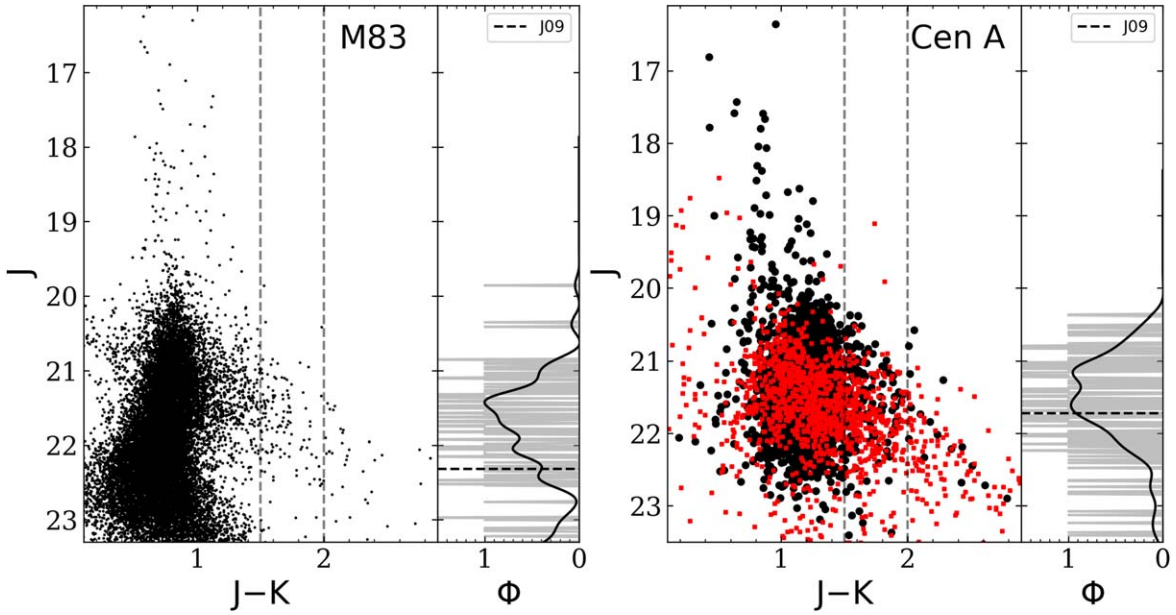

Figure A1. J vs. $(J-K)$ CMDs (left panels) and GLOESS-smoothed LFs in black overplotted on the binned LF in gray (right panels) for M83 and Cen A. There is no clearly defined peak in either LF. The dotted line represents the predicted JAGB luminosity from the EDD I-band TRGB distance modulus from J09, with a foreground extinction correction of $A_J = 0.05$ mag added for M83 and $A_J = 0.08$ mag for Cen A. Photometry of long-period variable stars from Rejkuba et al. (2003) is shown as red points in the CMD of Cen, showing that the location of the JAGB stars in our CMD is consistent with the location of the JAGB stars observed in Rejkuba et al. (2003).

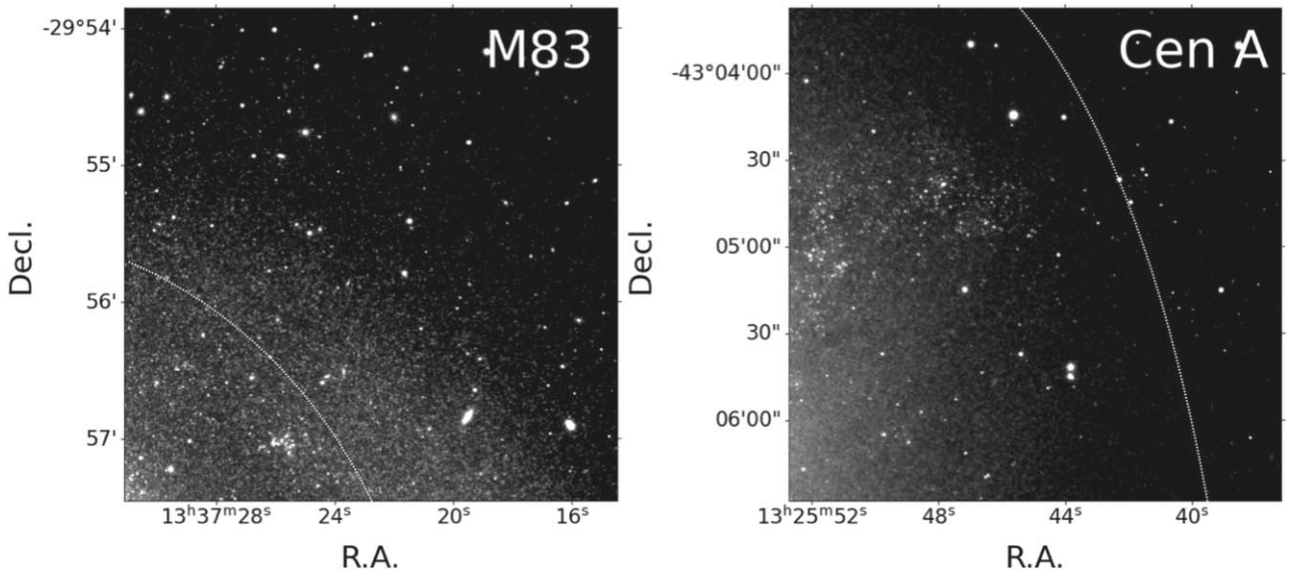

Figure A2. Images of M83 and Cen A observed with the FourStar camera on the 6.5 Magellan–Baade telescope. The JAGB measurements were measured outside the dotted white ellipse. In these two galaxies, we only observed the northwest quadrants of the galaxy.

Table A1
Literature Distances

Galaxy	Method	μ_0 (mag)	Reference	Notes
Cen A	JAGB method	27.95 ± 0.02	FM20	
Cen A	*I*-band TRGB	27.84 ± 0.04	J09	$m_{\rm F814W} = 23.97 \pm 0.03$ mag, $A_{\rm F814W} = 0.18$ mag
Cen A	Mira variables	27.96 ± 0.11	Rejkuba (2004)	
Cen A	Cepheids	27.67 ± 0.20	Ferrarese et al. (2007)	
M83	*I*-band TRGB	28.47 ± 0.05	J09	$m_{\rm F814W} = 24.52 \pm 0.03$ mag, $A_{\rm F814W} = 0.10$ mag
M83	Cepheids	28.25 ± 0.15	Thim et al. (2003)	

based distance of $\mu_0 = 27.67 \pm 0.20$ mag (Ferrarese et al. 2007) to the Mira-based distance of $\mu_0 = 27.96 \pm 0.11$ mag (Rejkuba 2004) (a difference of 0.5 Mpc!).

To perform an additional cross-check on our photometry of Cen A, we compared our photometry to the photometry of Rejkuba et al. (2003), who observed 1504 long-period variable stars using the ISAAC NIR imaging spectrometer at the ESO Paranal UT1 Antu 8.2 m telescope between 1999 and 2002 (332 of these stars have colors of 1.5 mag $< (J - K) < 2.0$ mag and are therefore JAGB stars). We overplot these stars in Figure A1, showing that the locations of our JAGB stars in the CMD are consistent with the locations of the JAGB stars observed in Rejkuba et al. (2003). Our photometry is likely not the source of the problem.

The magnitudes of the JAGB stars in Cen A are in the range 20.5 mag $< J <$ 23 mag, a significantly larger range of JAGB star magnitudes than what was seen for the 11 nearby galaxies in Figure 3, which was typically less than 1 mag. The large scatter of JAGB star magnitudes could therefore be due to Cen A's far distance (resulting in relatively larger photometry errors for the JAGB stars) or its complex star formation history.

A.2. M83

M83 is the farthest galaxy in our sample at around 4.9 Mpc (J09), with the second-farthest being NGC 1313 at about 4.0 Mpc away. We speculate that this is now the limit of where accurate JAGB distances can be measured with ground-based telescopes. Only two distances have recently been measured to M83, which range from 4.5 Mpc via Cepheid variables stars (Thim et al. 2003) to 4.9 Mpc via the *I*-band TRGB (J09). The lack of a clearly defined peak in the JAGB star LF indicates that the photometric scatter of the stars in this galaxy is significantly large, and that JAGB stars in galaxies at this distance may not be able to be accurately used as standard candles with ground-based telescopes.

Appendix B
T-band LFs and Edge Response Functions

In this section, the $T[J, (J, K)]$-band and $T[H, (J, K)]$-band LFs and edge detector response functions are shown in Figure B1.

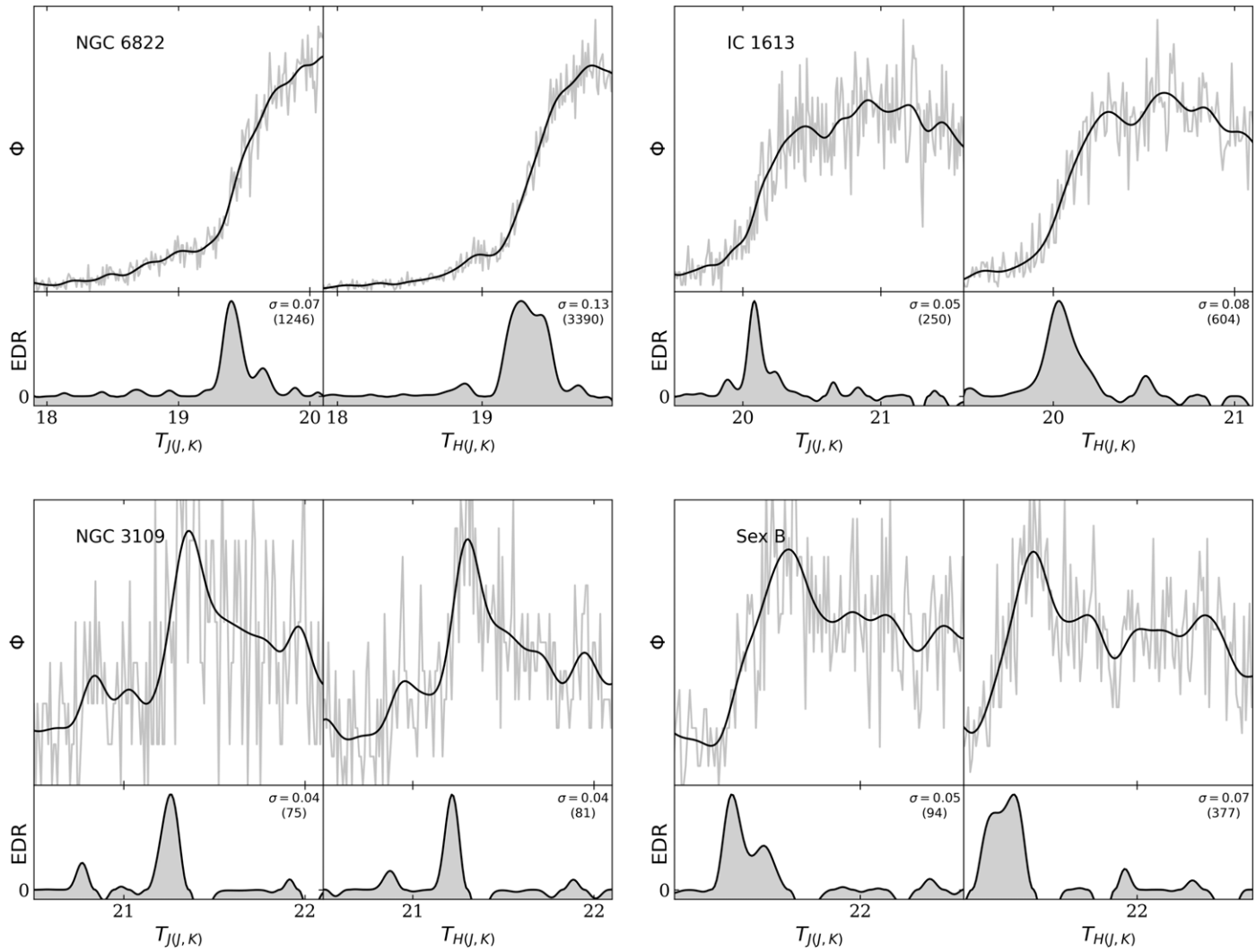

Figure B1. Rectified $T[J(J, K)]$ and $T[H(J, K)]$ LFs (top panels) and edge detector response functions (bottom panels) for the 10 galaxies with TRGB distances. All the data were transformed so that the TRGB is now insensitive to color. T-band magnitudes were binned using bins of 0.01 mag and then smoothed using a smoothing parameter of $\sigma_s = 0.10$ mag. The TRGB marks the point where the edge detector response is the largest, i.e., where the first derivative of the LF is the greatest. The measured width of the edge detector response, σ, and the number of TRGB stars contributing to the edge detector response are shown in the bottom panel of every figure.

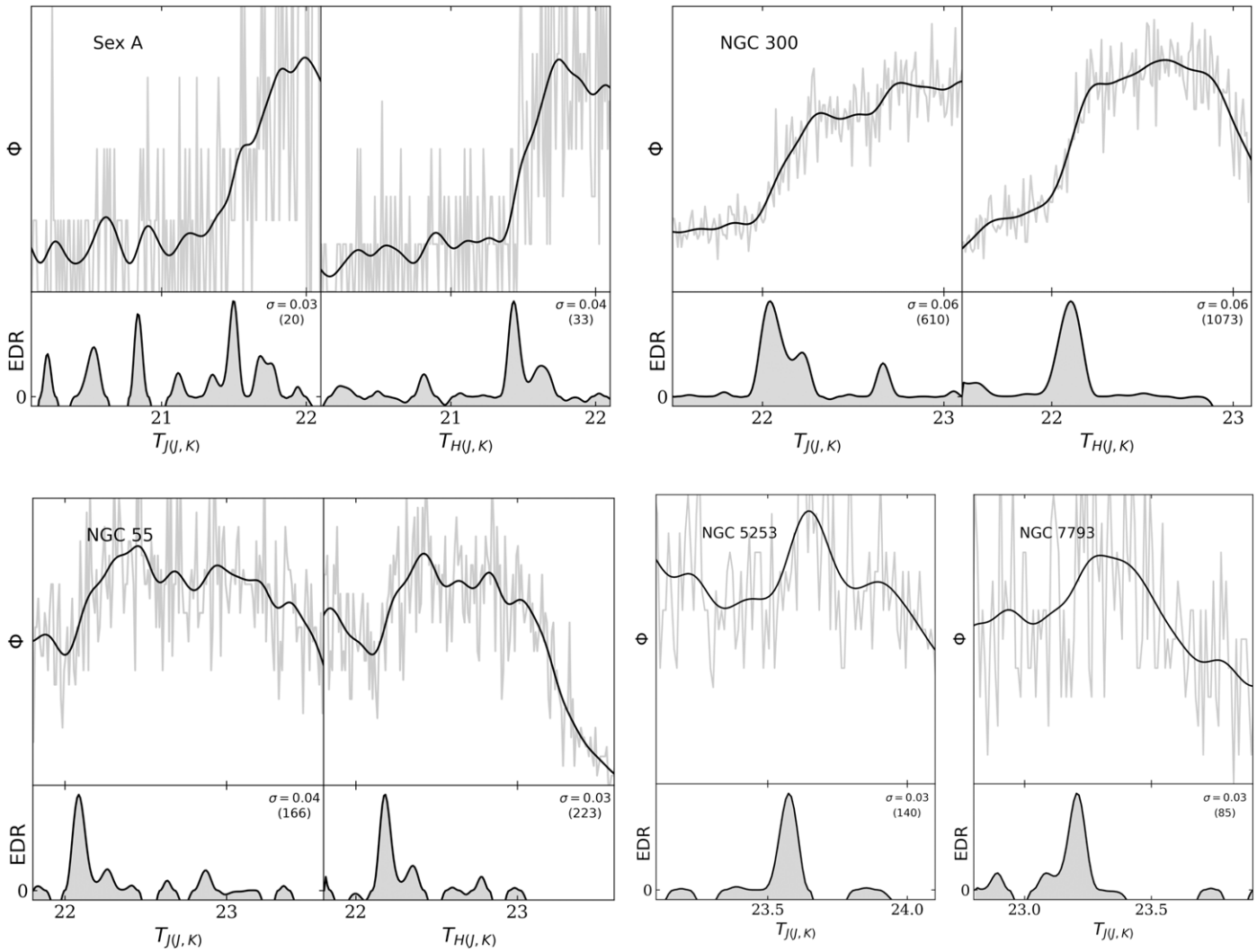

Figure B1. (Continued.)

ORCID iDs

Abigail J. Lee https://orcid.org/0000-0002-5865-0220
Andrew J. Monson https://orcid.org/0000-0002-0048-2586
Wendy L. Freedman https://orcid.org/0000-0003-3431-9135
Barry F. Madore https://orcid.org/0000-0002-1576-1676
Kayla A. Owens https://orcid.org/0000-0003-3339-8820
Tongtian Ren https://orcid.org/0000-0003-4988-3513

References

Anand, G. S., Rizzi, L., Tully, R. B., et al. 2021, AJ, 162, 80
Astropy Collaboration, Price-Whelan, A. M., Lim, P. L., et al. 2022, ApJ, 935, 167
Astropy Collaboration, Price-Whelan, A. M., Sipőcz, B. M., et al. 2018, AJ, 156, 123
Astropy Collaboration, Robitaille, T. P., Tollerud, E. J., et al. 2013, A&A, 558, A33
Beaton, R. L., Seibert, M., Hatt, D., et al. 2019, ApJ, 885, 141
Boyer, M. L., Pastorelli, G., Girardi, L., et al. 2024, arXiv:2401.14889
Cerny, W., Freedman, W. L., Madore, B. F., et al. 2020, arXiv:2012.09701
Cioni, M.-R. L., Irwin, M., Ferguson, A. M. N., et al. 2008, A&A, 487, 131
Cleveland, W. S., & Loader, C. 1996, in Proc. of the COMPSTAT '94 Satellite Meeting, Statistical Theory and Computational Aspects of Smoothing, ed. W. Härdle & M. G. Schimek (Heidelberg: Physica Heidelberg), 10
Cook, K. H., Aaronson, M., & Norris, J. 1986, ApJ, 305, 634
Dalcanton, J. J., Williams, B. F., Seth, A. C., et al. 2009, ApJS, 183, 67
Ferrarese, L., Mould, J. R., Stetson, P. B., et al. 2007, ApJ, 654, 186
Freedman, W. L. 2021, ApJ, 919, 16
Freedman, W. L., & Madore, B. F. 2020, ApJ, 899, 67
Freedman, W. L., Madore, B. F., Hoyt, T., et al. 2020, ApJ, 891, 57
Habing, H. J., & Olofsson, H. 2003, Asymptotic Giant Branch stars (New York: Springer)
Harris, C. R., Millman, K. J., van der Walt, S. J., et al. 2020, Natur, 585, 357
Harris, G. L. H. 2010, PASA, 27, 475
Hatt, D., Beaton, R. L., Freedman, W. L., et al. 2017, ApJ, 845, 146
Hoyt, T. J., Freedman, W. L., Madore, B. F., et al. 2018, ApJ, 858, 12
Hunter, J. D. 2007, CSE, 9, 90
Jacobs, B. A., Rizzi, L., Tully, R. B., et al. 2009, AJ, 138, 332
Jang, I. S., Hoyt, T. J., Beaton, R. L., et al. 2021, ApJ, 906, 125
Kamath, D., Dell'Agli, F., Ventura, P., et al. 2023, MNRAS, 519, 2169
Lee, A. J. 2023, ApJ, 956, 15
Lee, A. J., Freedman, W. L., Madore, B. F., et al. 2021a, ApJ, 907, 112
Lee, A. J., Freedman, W. L., Madore, B. F., et al. 2021b, ApJ, 923, 157
Lee, A. J., Rousseau-Nepton, L., Freedman, W. L., et al. 2022, ApJ, 933, 201
Lee, M. G., Freedman, W. L., & Madore, B. F. 1993, ApJ, 417, 553
Loader, C. 2004, Smoothing: Local Regression Techniques Working Paper No. 2004, Humboldt Univ. Berlin, https://www.econstor.eu/bitstream/10419/22186/1/12_cl.pdf
Madore, B. F., & Freedman, W. L. 2020a, ApJ, 899, 66
Madore, B. F., & Freedman, W. L. 2020b, AJ, 160, 170
Madore, B. F., Freedman, W. L., Hatt, D., et al. 2018, ApJ, 858, 11
Madore, B. F., Freedman, W. L., & Lee, A. J. 2022a, ApJ, 926, 153
Madore, B. F., Freedman, W. L., Lee, A. J., et al. 2022b, ApJ, 938, 125
Madore, B. F., Freedman, W. L., Owens, K. A., et al. 2023, AJ, 166, 2

Madore, B. F., Mager, V., & Freedman, W. L. 2009, ApJ, 690, 389
Marigo, P., Girardi, L., & Chiosi, C. 2003, A&A, 403, 225
Massey, P., Neugent, K. F., Levesque, E. M., et al. 2021, AJ, 161, 79
Mazzi, A., Girardi, L., Zaggia, S., et al. 2021, MNRAS, 508, 245
McKinney, W. 2010, in Proc. of the 9th Python in Science Conf., ed. S. van der Walt & J. Millman, 51
McQuinn, K. B. W., Boyer, M., Skillman, E. D., et al. 2019, ApJ, 880, 63
Melbourne, J., & Boyer, M. L. 2013, ApJ, 764, 30
Monson, A. J., Beaton, R. L., Scowcroft, V., et al. 2017, AJ, 153, 96
Nikolaev, S., & Weinberg, M. D. 2000, ApJ, 542, 804
Parada, J., Heyl, J., Richer, H., et al. 2021, MNRAS, 501, 933
Parada, J., Heyl, J., Richer, H., et al. 2023, MNRAS, 522, 195
Pastorelli, G., Marigo, P., Girardi, L., et al. 2020, MNRAS, 498, 3283
Persson, S. E., Madore, B. F., Krzemiński, W., et al. 2004, AJ, 128, 2239
Persson, S. E., Murphy, D. C., Smee, S., et al. 2013, PASP, 125, 654
Qing, G., Wang, W., Liu, J.-F., et al. 2015, ApJ, 799, 19
Rejkuba, M. 2004, A&A, 413, 903
Rejkuba, M., Minniti, D., & Silva, D. R. 2003, A&A, 406, 75
Rich, J. A., Persson, S. E., Freedman, W. L., et al. 2014, ApJ, 794, 107
Richer, H. B. 1981, ApJ, 243, 744
Ripoche, P., Heyl, J., Parada, J., et al. 2020, MNRAS, 495, 2858
Salaris, M., & Cassisi, S. 1997, MNRAS, 289, 406
Schlafly, E. F., & Finkbeiner, D. P. 2011, ApJ, 737, 103
Schlegel, D. J., Finkbeiner, D. P., & Davis, M. 1998, ApJ, 500, 525
Scowcroft, V., Freedman, W. L., Madore, B. F., et al. 2013, ApJ, 773, 106
Secchi, A. 1868, Mem. Soc. Ital. Scienze, 2, 73
Skrutskie, M. F., Cutri, R. M., Stiening, R., et al. 2006, AJ, 131, 1163
Stetson, P. B. 1987, PASP, 99, 191
Tammann, G. A., Reindl, B., & Sandage, A. 2011, A&A, 531, A134
Thim, F., Tammann, G. A., Saha, A., et al. 2003, ApJ, 590, 256
Tully, R. B., Rizzi, L., Shaya, E. J., et al. 2009, AJ, 138, 323
Virtanen, P., Gommers, R., Oliphant, T. E., et al. 2020, NatMe, 17, 261
Weinberg, M. D., & Nikolaev, S. 2001, ApJ, 548, 712
Zgirski, B., Pietrzyński, G., Gieren, W., et al. 2021, ApJ, 916, 19